The vertical structure of the circulation and dynamics in Hudson Shelf Valley

Steven J. Lentz[1], Bradford Butman[2], and Courtney Harris[3]

[1]Woods Hole Oceanographic Institution, Woods Hole, Massachusetts, USA, [2]US Geological Survey, Woods Hole Coastal and Marine Science Center, Woods Hole, Massachusetts, USA, [3]Department of Physical Sciences, Virginia Institute of Marine Science, Gloucester Point, Virginia, USA

Abstract Hudson Shelf Valley is a 20–30 m deep, 5–10 km wide v-shaped submarine valley that extends across the Middle Atlantic Bight continental shelf. The valley provides a conduit for cross-shelf exchange via along-valley currents of 0.5 m s^{-1} or more. Current profile, pressure, and density observations collected during the winter of 1999–2000 are used to examine the vertical structure and dynamics of the flow. Near-bottom along-valley currents having times scales of a few days are driven by cross-shelf pressure gradients setup by wind stresses, with eastward (westward) winds driving onshore (offshore) flow within the valley. The along-valley momentum balance in the bottom boundary layer is predominantly between the pressure gradient and bottom stress because the valley bathymetry limits current veering. Above the bottom boundary layer, the flow veers toward an along-shelf (cross-valley) orientation and a geostrophic balance with some contribution from the wind stress (surface Ekman layer). The vertical structure and strength of the along-valley current depends on the magnitude and direction of the wind stress. During offshore flows driven by westward winds, the near-bottom stratification within the valley increases resulting in a thinner bottom boundary layer and weaker offshore currents. Conversely, during onshore flows driven by eastward winds the near-bottom stratification decreases resulting in a thicker bottom boundary layer and stronger onshore currents. Consequently, for wind stress magnitudes exceeding 0.1 N m^{-2}, onshore along-valley transport associated with eastward wind stress exceeds the offshore transport associated with westward wind stress of the same magnitude.

1. Introduction

Hudson Shelf Valley is a 20–30 m deep submarine valley that extends across the continental shelf of the Middle Atlantic Bight from near the mouth of the Hudson River to the outer shelf (Figures 1 and 2). It is the only submerged river valley on the continental shelf of the Middle Atlantic Bight that has not been filled with sediment. Cross-shelf (along-valley) flows are much stronger within Hudson Shelf Valley than cross-shelf flows on the adjacent shelf [*Nelsen et al.*, 1978; *Mayer et al.*, 1982; *Manning et al.*, 1994; *Harris et al.*, 2003]. Consequently, Hudson Shelf Valley, like many submarine valleys and canyons, may provide an important conduit for cross-shelf exchange [*Allen and de Madron*, 2009]. This has led to studies focused on Hudson Shelf Valley's influence on the New York Bight shelf circulation [*Han et al.*, 1980; *Gong et al.*, 2010], dispersal of freshwater from Hudson River [*Chant et al.*, 2008; *Zhang et al.*, 2009], sediment transport [*Freeland et al.*, 1981; *Manning et al.*, 1994; *Harris et al.*, 2003], and pollutant transport from the New York City offshore dump site located near the head of the valley [*Manning et al.*, 1994].

Previous studies of Hudson Shelf Valley have observed near-bottom along-valley flows of 0.4 m s^{-1} or more associated with strong east-west winds [*Lavelle et al.*, 1975; *Nelsen et al.*, 1978; *Mayer et al.*, 1982; *Manning et al.*, 1994; *Harris et al.*, 2003]. Eastward winds drive near-bottom onshore flows in the valley, while westward winds drive offshore flows. *Lavelle et al.* [1975] hypothesized that eastward (westward) winds resulted in a wind-driven setdown (setup) near the coast, and the resulting cross-shelf pressure gradient forced the onshore (offshore) near-bottom flow in the valley. Early numerical modeling studies support this description of the dynamics [*Hsueh*, 1980; *Hsueh et al.*, 1984]. While previous studies have related flow in Hudson Shelf valley to coastal sea level variations [e.g., *Harris et al.*, 2003], the along-valley pressure gradient has not been estimated to directly test the hypothesized dynamics.

Mean flows over time scales of months in Hudson Shelf Valley tend to be onshore [*Nelsen et al.*, 1978; *Mayer et al.*, 1982; *Manning et al.*, 1994; *Harris et al.*, 2003] (Figures 1 and 2), qualitatively consistent with the mean
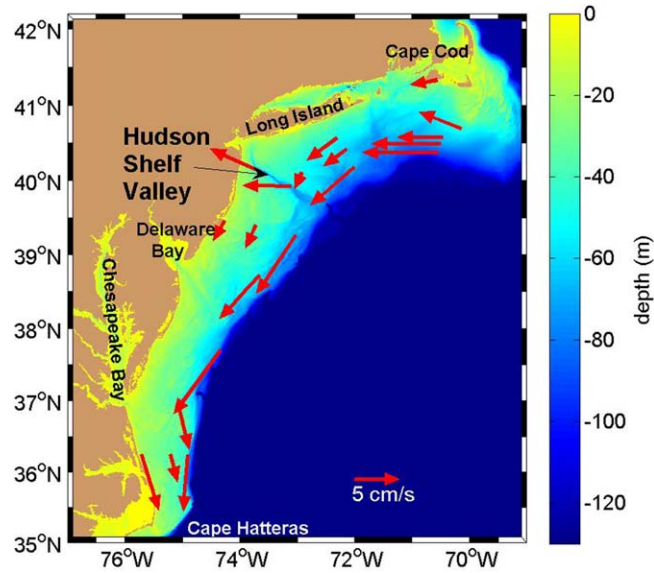
Figure 1. Middle Atlantic Bight bathymetry and the mean depth-averaged shelf currents from long-term moorings [from *Lentz*, 2008a]. Note the onshore mean currents in excess of 5 cm s^{-1} in Hudson Shelf Valley.

eastward winds [*Lentz*, 2008a] or the tendency for an asymmetry that favors onshore flow in canyons [*Klinck*, 1996]. However, the "mean" flows cited in previous studies have generally spanned months and it is not known whether there is a consistent seasonal cycle in the Hudson Shelf Valley currents because there have not been time series spanning several years. The vertical structure of the flow within the valley and how it depends on stratification and other factors has not been described because most previous studies have collected current measurements either near the bottom [*Manning et al.*, 1994] or at only a few heights above the bottom [*Mayer et al.*, 1982] without simultaneous density observations.

While observations of strong flows in submarine canyons and valleys resulting in substantial cross-shelf or cross-slope transport extend back at least to the late 1960's when reliable current meters were first developed [*Shepard et al.*, 1969], a consistent qualitative picture of the dynamics has only begun to emerge in the last two decades (see *Allen and de Madron* [2009] for a more complete review). Early theoretical studies showed how the cross-shelf pressure gradient associated with geostrophic along-shelf flows could drive substantial cross-shelf (along-canyon) flows in a narrow slot canyon since there can be no along-shelf flow within the canyon and hence no Coriolis force to balance the cross-shelf pressure gradient [*Freeland and Denman*, 1982; *Klinck*, 1989]. Subsequent numerical modeling studies in more realistic geometries revealed an asymmetry in the canyon response to upwelling and downwelling-favorable along-slope flows [*Klinck*, 1996; *She and Klinck*, 2000; *Kämpf*, 2006], presumably associated with the response of coastal-trapped waves (Rossby or Kelvin waves) to the topographic perturbation [e.g., *Johnson*, 1978; *Killworth* 1978; *Allen and de Madron*, 2009; *Kampf*, 2012]. An asymmetry was also observed in a model study of Hudson Shelf Valley [*Harris and Signell*, 1999]. *Klinck* [1996] found that upwelling-favorable along-slope flows (in the opposite direction of Kelvin-wave propagation) drive stronger canyon flows than downwelling-favorable along-slope flows of the same magnitude. For upwelling conditions, the along-slope
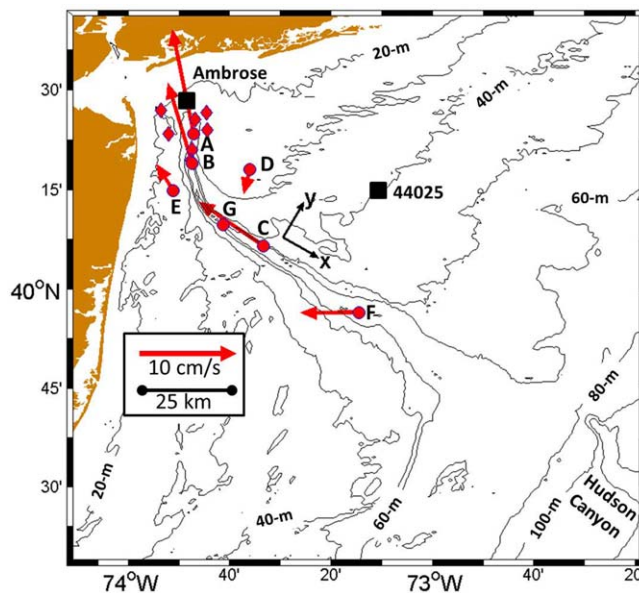

Figure 2. Hudson Shelf Valley bathymetry map showing locations of USGS (circles) and NMFS (diamonds) current measurement sites, and Ambrose tower and NDBC buoy 44025 meteorological measurement sites. Mean current vectors 5 mab from the winter 1999–2000 USGS deployment are also shown. An along-valley *x* and cross-valley *y* coordinate system is used with the along-valley orientation defined at each site based on the major axis of the low-frequency currents 5 mab.

flow is deflected up the canyon and concentrated farther up the slope on the downstream side of the canyon [*Klinck*, 1996; *Allen*, 1996]. Downwelling conditions result in a more symmetric response, with the flow deflected slightly onshore and then offshore as it passes over the canyon. In laboratory studies of zero-mean oscillatory flows over canyons, this asymmetry in the response to upwelling versus downwelling conditions can result in a net upwelling [*Boyer et al.*, 2004; *Boyer et al.*, 2006]. Though in a numerical modeling study, *Kampf* [2009] suggests that purely oscillatory flow does not produce a significant net onshore transport of dense water. Numerical modeling studies also indicate that stratification can limit the vertical extent of the topographic influence of the canyon [*Allen and Hickey*, 2010; *Klinck*, 1996]. Stronger stratification can also result in an along-canyon density gradient that tends to balance the sea surface slope [*She and Klinck*, 2000] and reduce the along-canyon transport during upwelling [*Kämpf*, 2007; *Mirshak and Allen*, 2005]. Most of the numerical modeling and laboratory studies cited above have focused on geometries consistent with canyons in deep water over continental slopes, as have many of the observational studies of canyons [e.g., *Allen and de Madron*, 2009, though see *Hickey*, 1997]. The relevance of the previous work focusing on canyons that incise continental slopes to shallower, narrow submarine valleys that incise continental shelves, like the Hudson Shelf Valley, is unclear. For example, numerical modeling studies of Hudson Shelf Valley [*Hsueh*, 1980; *Hsueh et al.*, 1984] suggest bottom stress is an important component of the dynamics, in contrast to numerical modeling studies of deeper continental slope canyons where frictional effects are thought to be of minor importance [e.g., *Kämpf*, 2006, 2007].

Observations from a field program to study sediment transport in Hudson Shelf Valley [*Butman et al.*, 2003a; *Harris et al.*, 2003] are used to characterize the vertical structure of the along-valley flow, estimate the along-valley (cross-shelf) transport, and investigate the dynamics of the flow in Hudson Shelf Valley. This data set has several advantages over previous studies, notably more complete vertical coverage of current profiles and observations that allow estimation of terms in the along-valley momentum balance. Bottom pressure and density time series from several sites along the valley (sites A, B, C, and F in Figures 2 and 3) provide estimates of the along-valley pressure gradient, the along-valley density gradient, and the stratification. High-frequency, near-bottom current measurements provide estimates of bottom stress [*Harris et al.*, 2003]. Current observations from two previous studies, the 1974–1978 Marine Ecosystem Analysis project (MESA) in the New York Bight [*Mayer et al.*, 1982; *Mayer*, 1982] and a study of sediment transport at the New York Bight 12 mile dumpsite near the head of the valley [*Manning et al.*, 1994], are also examined to provide a more complete description of the circulation, including seasonal variability, and the relationship between the wind stress and the along-valley flow.

2. Site, Observations, and Processing

2.1. Hudson Shelf Valley

Hudson Shelf Valley is the submerged ancestral Hudson River Valley that extends from near the mouth of the present Hudson River to the outer continental shelf [*Butman et al.*, 2003b; *Thieler et al.*, 2007]. The valley is oriented roughly northwest-southeast (120°N) over the mid and outer shelf, curving to a north-south (0°N) orientation near the head of the valley in the apex of the New York Bight (Figure 2). The valley is about 5 km wide from the head to midshelf, and then broadens to a submerged delta near the outer edge of the continental shelf. Consequently, the valley is not evident near the shelfbreak and not clearly connected with Hudson Canyon that incises the continental slope [*Keller et al.*, 1973].

The floor of the valley is steeper at its landward side and flattens offshore, with six enclosed depressions, 5–10 km long and 5–15 m deep along the valley axis (Figure 3). The valley floor deepens from about 30 m at the head to 70 m at site C, an along-valley distance of about 50 km. From site C to the shelfbreak (about 100 km), the depth of the valley floor fluctuates between 70 and 90 m. There are relic sand waves with amplitudes of about 1–5 m between sites M16 and M18 (Figure 3) [*Butman et al.*, 2003b; *Thieler et al.*, 2007]. The valley is 20–30 m deeper than the surrounding shelf (dashed line, Figure 3) between sites B and F.

2.2. Field Programs
2.2.1. United States Geological Survey (USGS) Studies

The focus of this study is an array of instrumented tripods and moorings deployed at six sites in and around Hudson Shelf Valley from early December 1999 through mid-April 2000 (Figure 2). Sites A, B, C, and F were located along the axis of the valley in water depths of 38, 55.5, 69.5, and 74 m, respectively (Figure 3). Sites
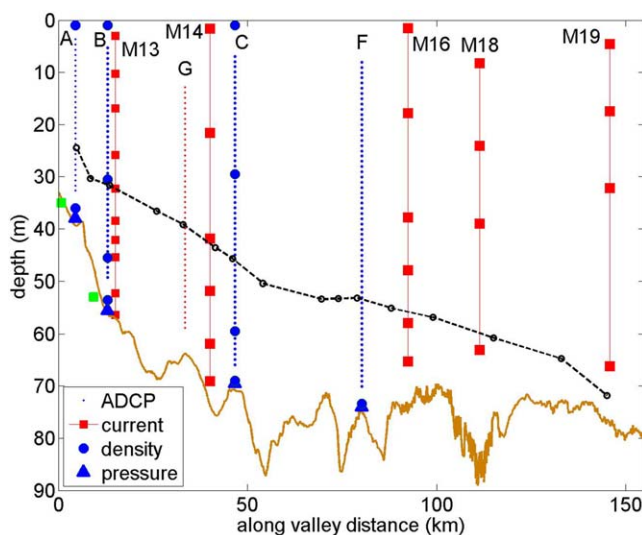
Figure 3. Section along the axis of Hudson Shelf Valley showing the bathymetry from USGS survey [*Butman et al.*, 2003b] and the instrument locations for the mooring sites in the valley. Current meters are VACMs (green squares), Anderaas (red squares), or RDI ADCPs (blue or red dots). The dashed line is an estimate of the depth of the valley rim based on cross-valley sections (at open circles) from USGS bathymetry survey. Site locations are shown in Figures 2 and 4.

C and F were on topographic highs between depressions. Sites D and E were on either side of the valley on the 25 m isobath. Bottom-mounted, upward-looking RD Instruments 300 kHz Workhorse Acoustic Doppler Current Profilers (ADCP) were deployed at all six sites. The ADCPs measured current profiles with 1 m vertical resolution from about 5 mab (meters above the bottom) to within 3.5–8 m of the surface depending on the water depth (Figure 3). Current measurements 0.4 mab (sites A, B, C, D, E) and 1 mab (sites A, B, D) were obtained using Benthic Acoustic Stress Sensors or Modular Acoustic Velocity Sensors mounted on bottom tripods. The ADCPs and near-bottom current meters collected 5 min burst averages of 1 Hz samples every 15 min.

Bottom pressure measurements were obtained at all six sites using Paroscientific Digiquartz pressure sensors recording 5 min averages. The pressure time series at site A is only 2 months long. Temperature and conductivity were sampled every 5 min using SeaBird sensors deployed at 1 m depth (except at F) and near the bottom at each site, at 30.5 and 45.5 m depth at site B, and at 29.5 and 59.5 m depth at site C (Figure 3). A more complete description of the field program is given in *Butman et al.* [2003a] and *Harris et al.* [2003].

In a subsequent spring field program, carried out in collaboration with Rutgers University, upward-looking 300 kHz ADCPs were deployed along the axis of Hudson Shelf Valley from early April to mid-June 2006 at sites A and G (Figures 2 and 3). Site G was located 13 km onshore of site C in 62 m of water. The vertical and temporal sampling was the same as for the winter 1999–2000 ADCPs.

Figure 4. Map showing locations of MESA sites and subtidal principal axes ellipses for near-bottom (1–5 mab) currents. Current ellipse at M18 is from current meter 14 mab.

2.2.2. Marine Ecosystem Analysis Project (MESA)
Current observations collected between 1974 and 1978 from 29 sites in the New York Bight (Figure 4) as part of the **Marine Ecosystem Analysis project** [*Mayer et al.*, 1982; *Mayer*, 1982] were obtained from the National Ocean Data Center archive. Moorings at each site supported 2–8 Aanderaa current meters typically sampling currents and temperatures at 20 or 30 min intervals for single or multiple deployments of 1–3 months. Of particular interest for this study are observations from five sites within Hudson Shelf Valley: M13 (total record lengths 49–123 days), M14 (154–361 days), M16 (105–370 days), M18 (46–113 days), and M19 (43–65 days).
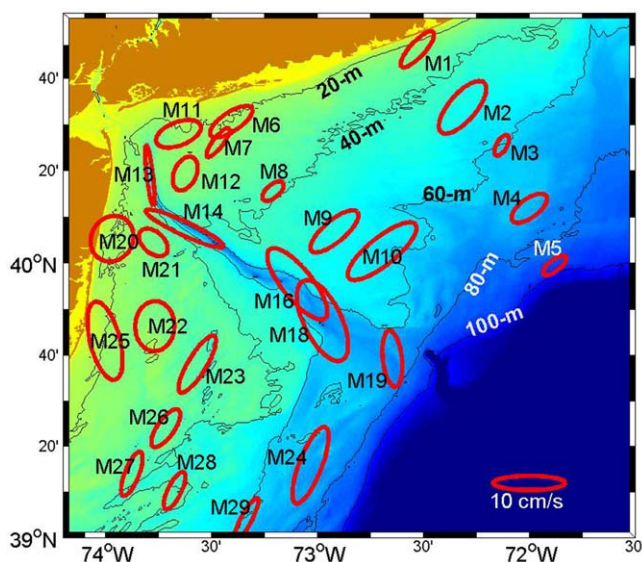
2.2.3. National Marine Fisheries Service (NMFS) Study

As part of a National Marine Fisheries Service study of the New York City sewage dumpsite 12 miles east of Sandy Hook, New Jersey, near-bottom current observations were obtained from seven sites near the head of Hudson Shelf Valley during the summer of 1987 and from May 1988 to June 1989 [*Manning et al.*, 1994]. Single Vector-Averaging Current Meters (VACMs) were deployed 1–4 mab at each site for 2 months to a year (Figure 2). Two of the sites were in Hudson Shelf Valley (Figure 3).

2.2.4. Ancillary Data

Wind stress was estimated from wind velocity from National Data Buoy Center (NDBC) buoy 44025 (Figure 2) using a bulk formula assuming neutral conditions [*Fairall et al.*, 2003]. The oceanographic convention is used for wind direction, i.e., an eastward wind blows toward the east. Gaps in the wind stress time series from 44025 were filled with wind-stress estimates from Ambrose tower. Correlations between the two wind stress time series were 0.90 for the east-west component and 0.85 for the north-south component.

A total of 314 CTD (conductivity-temperature-depth) profiles within 2 km of the axis of Hudson Shelf Valley were extracted from the National Ocean Data Center historical hydrographic database to characterize the annual variation in stratification in the valley. Approximately one third of the profiles were near the head of the valley (latitude $> 40°15'$N), with the remaining two thirds evenly distributed along the rest of the valley.

2.3. Data Processing

All time series were block-averaged to hourly values. The current velocity time series contain substantial variability at both tidal and subtidal frequencies. The focus here is on the subtidal variability, so a low-pass filter having a 33 h half-power point was applied to the time series. Pressure time series were detided using t-tide [*Pawlowicz et al.*, 2002] before low-pass filtering. Terms in the along-valley momentum balance are estimated from the unfiltered hourly values and then low-pass filtered (see Appendix A). For most of the analysis, an along-valley coordinate system was adopted with x being the along-valley direction (positive offshore), and y the cross-valley (positive toward the north and east; Figure 2). At each of the shelf valley sites, the along-valley orientation was defined as the direction of the principal axis of the subtidal flow 5 mab. All references in this paper to along-valley flow at individual stations are rotated into this local coordinate system. The along-valley pressure gradient at site C was estimated as the pressure at site F minus the pressure at site B. (The depths of the bottom pressure sensors relative to the geoid are not known accurately enough to determine the mean pressure gradient so the mean pressure gradient when near-bottom current speeds were less than 5 cm s^{-1} was set to zero.) Estimation of the pressure gradient and other terms in the along-valley momentum balance are described in the Appendix A.

The ADCP current measurements are thought to have an accuracy of a few cm s^{-1} [*Plueddemann et al.*, 2003; *Pettigrew et al.*, 1986]. The MESA current measurements using Aanderaa current meters are less accurate, especially in the presence of surface gravity wave velocities [*Beardsley et al.*, 1981].

The decorrelation time scale is approximately 36 h for the subtidal along-valley flow and 24 h for the cross-valley flow based on the first zero-crossing of the autocorrelation function from the USGS and MESA current time series. Thus, there are about 20 independent samples per month.

3. Overview of the Near-Bottom Flow in Hudson Shelf Valley

3.1. Subtidal Variability

Subtidal current variability within Hudson Shelf Valley is dominated by strong along-valley flow events having time scales of days (Figure 5b). Near-bottom subtidal current variability is strongly polarized along the valley axis (compare black and red lines in Figure 5b), with major axis amplitudes of about 0.15 m s^{-1} and minor axis amplitudes of $\sim$0.03 m s^{-1} (Figure 4). Near-bottom subtidal along-valley (cross-shelf) flows are about a factor of five larger than subtidal cross-shelf flows on the adjacent shelf (Figure 4). Subtidal along-valley currents are significantly correlated along the valley; the correlation between near-bottom currents at the USGS valley sites that are farthest apart, sites A and F (separation 80 km) is 0.8. (All reported correlations are significantly different from zero at the 95% confidence level unless noted otherwise.)

The near-bottom subtidal, along-valley flow is significantly correlated with the wind stress at all sites within Hudson Shelf Valley in all three studies (Figure 6a, also compare black lines in Figure 5a and
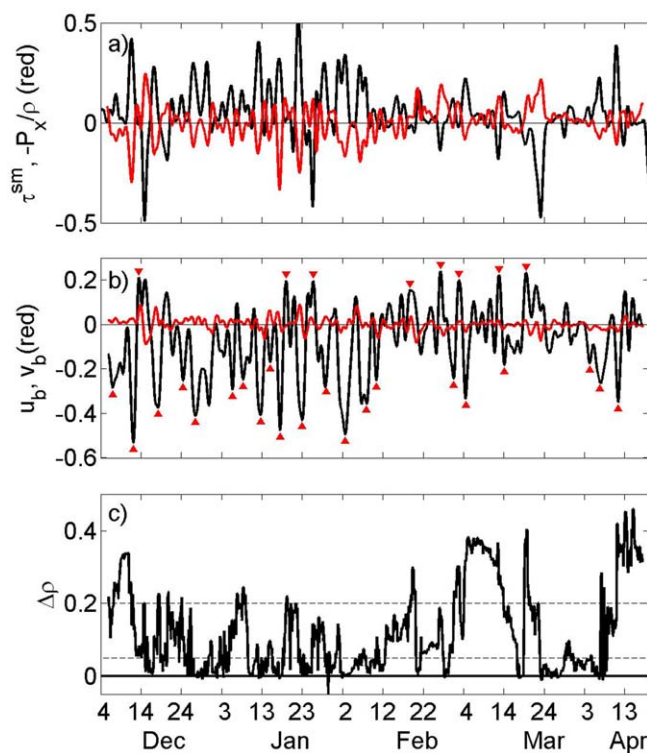
Figure 5. Time series of the (a) low-passed wind stress (N m^{-2}) and along-valley pressure gradient (10^{-4} m s^{-2}, red), (b) low-passed near-bottom along-valley and cross-valley (red) currents (m s^{-1}) at site C, and (c) density difference (kg m^{-3}) between 0.5 and 40 mab at site C. Wind stress orientation is positive toward 110°T and leads currents by 10 h. Pressure gradient is estimated as difference between sites B and F. The 28 events when the subtidal along-valley current at 5 mab exceeded 0.15 m s^{-1} are noted by triangles in Figure 5b. Dashed lines in Figure 5c indicates $\Delta\rho = 0.05$ kg m^{-3} and $\Delta\rho = 0.2$ kg m^{-3} used to define unstratified and stratified profiles.

Figure 5b). Maximum correlation is with the approximately east-west component of the wind stress (orientation 90°T–120°T; degrees clockwise relative to true north), so eastward (offshore) wind stresses force onshore flow in the valley and westward wind stresses force offshore flow, as noted in previous studies [*Lavelle et al.*, 1975; *Nelsen et al.*, 1978; *Mayer et al.*, 1982; *Manning et al.*, 1994; *Harris et al.*, 2003]. Consequently, maximum correlations and regressions slopes are reported as negative since wind and currents tend to be roughly in opposite directions. Maximum (negative) correlations generally range from −0.7 to −0.85 with the wind stress leading the along-valley flow by about 10 h. The regression slope range is −0.7 to −1.7 m s^{-1}/N m^{-2} (Figure 6b), with the suggestion of lower values inshore and offshore where the valley broadens and the flow is less confined by the bathymetry (Figure 2). Intercepts are typically around −0.02 m s^{-1} (Figure 6c), though often not significantly different from zero, suggesting the possibility of a weak onshore flow in the valley in the absence of wind forcing. Based on the consistency of the empirical relationship between wind stress and near-bottom along-valley current (Figure 6), we define τ^{sm} (maximum correlation with near-bottom along-valley current) as the wind stress having an orientation of 110°T and leading the near-bottom current by 10 h. The wind stress orientation that results in maximum correlation is not along-shelf, though it is hard to define along-shelf in this region since the coastline orientation changes by almost 90° near the head of the valley. The wind stress orientation that is most highly correlated with the along-shelf currents either west or south of Hudson Shelf Valley is approximate 50°T (from MESA data). This is similar to the wind stress orientation that is most highly correlated with the along-shelf current on the New England shelf and generally reflects an average along-shelf orientation of the central portion of Middle Atlantic Bight stretching from Cape Cod to Chesapeake Bay [*Noble et al.*, 1983; *Beardsley et al.*, 1985] (see *Shearman and Lentz* [2003] for discussion of this).

Time series of the along-valley pressure gradient (Figure 5a, red line) during the USGS winter deployment support the basic idea proposed by *Lavelle et al.* [1975] that the wind stress sets up a cross-shelf pressure gradient that forces the along-valley flow. The along-valley (cross-shelf) pressure gradient is significantly correlated with the wind stress (Figure 5a). The maximum correlation is 0.83 with the pressure gradient lagging the wind stress by 3 h and a wind stress orientation of 110°T. The near-bottom along-valley flow is, in turn, correlated with the along-valley pressure gradient (correlations −0.80 to −0.66, open squares in Figure 6a) with the near-bottom current lagging the pressure gradient by about 6–11 h. The correlations between the near-bottom currents and the along-valley pressure gradient are similar to the correlations between the near-bottom currents and the wind stress (compare squares with other symbols in Figure 6a). The dynamics of the along-valley flow are examined in section 4.3.

3.2. Seasonal Variation

Combining monthly means of the near-bottom along-valley flow from the USGS, MESA, and NMFS studies reveals a clear seasonal variation (Figure 7a). Monthly mean along-valley currents are consistently onshore at 0.05–0.15 m s^{-1} in winter (December to February; e.g., Figure 2) and near zero in late spring and summer (May through September). Monthly mean near-bottom cross-valley flows (not shown) are typically between ± 0.02 m s^{-1} and do not differ significantly from zero. This seasonal variation is in contrast to the surrounding Middle Atlantic Bight shelf, where the monthly mean flows are along-shelf toward the southwest at 0.05–0.15 m s^{-1} (Figure 1) with less seasonal variation [*Beardsley and Boicourt*, 1981; *Lentz*, 2008a, 2008b].

The monthly mean along-valley currents from all three studies are significantly correlated (0.71) with the monthly mean wind stress with essentially the same regression slope (-0.82 ± 0.37 m s^{-1}/N m^{-2}) and maximum correlation at the same wind stress orientation (110°T) found for the subtidal variability. This indicates that variations in the monthly mean wind stress account for about half the variance in the monthly means of the along-valley flow seen in Figure 7a. An average annual cycle of the along-valley flow was estimated from historical wind stresses at NDBC 44025 and Ambrose between 1985 and 2012 (black dashed line, Figure 7a) using a regression slope of -1 m s^{-1}/N m^{-2}, an intercept of -0.02 m s^{-1}, and a wind stress orientation of 110°T (Figure 6). The observed annual variation in the along-valley monthly mean currents is similar to the estimate of the annual cycle based on the wind stress, suggesting the limited current observations provide a reasonable description of the average annual cycle (compare dashed line and symbols in Figure 7a). In summer, the wind-stress estimate suggests a stronger (-0.02 m s^{-1}) onshore monthly mean flow than the limited current observations. The intercept may vary seasonally and be closer to zero in summer since monthly mean wind stresses during the summer 1988–1989 NMFS observations are similar to the 27 year summer mean wind stresses but the monthly mean along-valley currents during the NMFS study are near zero. The December 1999 to January 2000 period of the USGS observations had stronger southwestward winds than any year in the 1985–2002 period [*Harris et al.*, 2003], possibly accounting for the large up-canyon flows in December and January in the USGS data (Figure 7a).
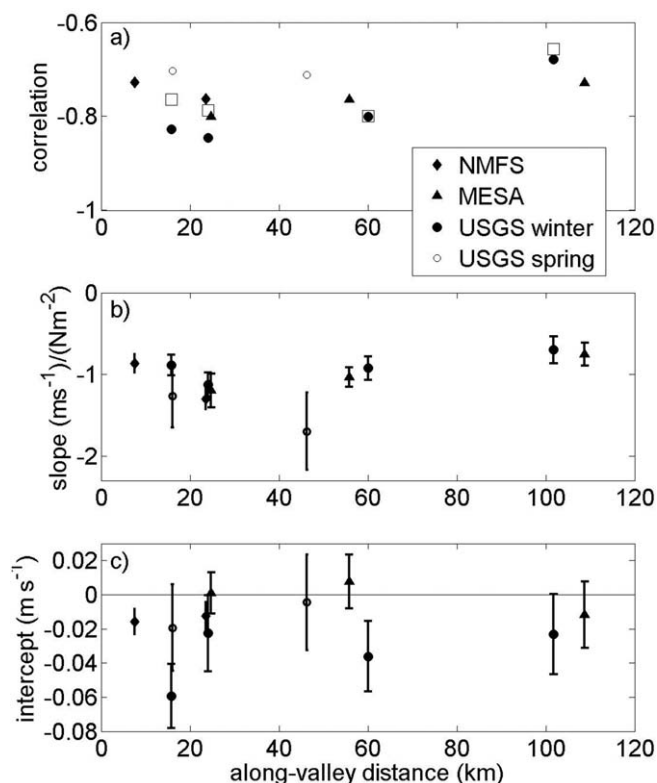

Figure 6. Results of a linear regression analysis of the form $u_b = a\tau^{sm} + b$, where τ^{sm} is subtidal wind stress (orientation 110°T, leads currents by 10 h) and u_b is along-valley flow 5 mab as a function of along-valley distance for NMFS, MESA, and USGS studies: (a) correlation, (b) regression slope a, and (c) intercept b. Error bars in Figures 6b and 6c are 95% confidence intervals. Open squares in Figure 6a are maximum correlations between along-valley pressure gradient and u_b, with pressure gradient leading current by about 8 h.

4. Subtidal Along-Valley Flow Characteristics and Dynamics

4.1. Vertical Structure Flow

The vertical structure of the flow in and above Hudson Shelf Valley depends on both the stratification and the direction of the along-valley flow. Stratification in the vicinity of Hudson Shelf Valley has a large annual variation consistent with the rest of the Middle Atlantic Bight [*Beardsley et al.*, 1985; *Lentz et al.*, 2003]. In winter, the water column both within and above the valley is typically unstratified or weakly stratified
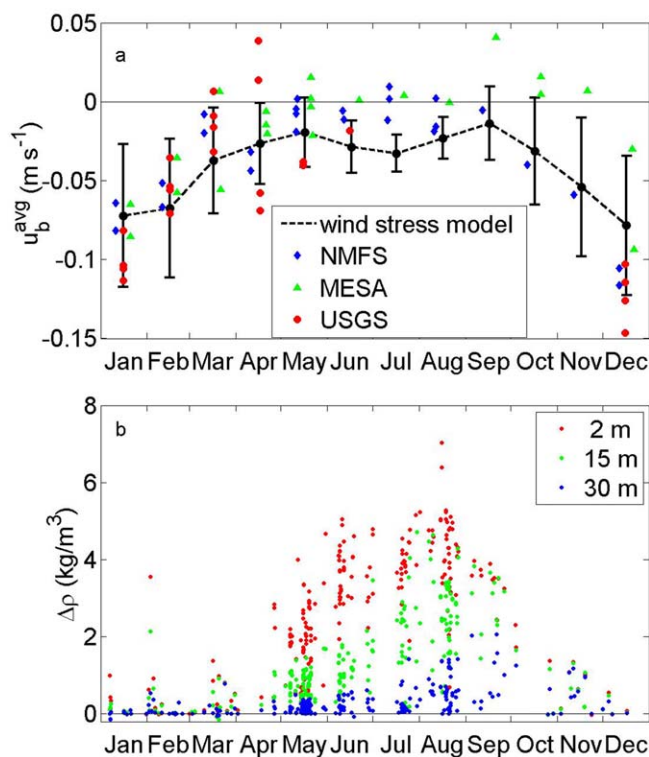
Figure 7. (a) Monthly means of observed near-bottom along-valley currents from MESA, NMFS, and USGS studies (points for NMFS and MESA offset from center of month to avoid overlap) and monthly means of near-bottom currents estimated using 1985–2012 wind stresses from NDBC 44025 and Ambrose (dashed line) and (b) near-bottom water density minus the density at depths of 2, 15, and 30 m below the surface from individual profiles obtained within 2 km of the valley axis (from the National Ocean Data Center historical hydrographic database). The empirical wind stress model is $u_b = a\tau^{sm} + b$, with $a = -1\,\text{m s}^{-1}/\text{N m}^{-2}$, $b = -0.02\,\text{m s}^{-1}$ and error bars indicate standard deviations of 20 monthly means. Only months with 20 or more days of near-bottom current observations are shown in Figure 7a.

(Figure 7b). Stratification above the valley increases in spring due to the development of the seasonal thermocline [*Bigelow*, 1933] and pooling of the Hudson River discharge in the New York Bight [*Castelao et al.*, 2008]. Within the valley (blue dots, Figure 7b), the strongest stratification occurs in late summer and fall, presumably as the seasonal thermocline and low-salinity near-surface water are mixed downward by storms [e.g., *Lentz et al.*, 2003].

To examine the dependence of the vertical structure of the flow on water-density stratification and flow direction, we focus on site C from the USGS December 1999 to April 2000 deployment because there are density time series at four heights spanning most of the water column (Figure 3). Site C is also in a nearly linear section of the valley (Figure 2) that is deep relative to the adjacent shelf (Figure 3). Results are similar for site B, where there are also density time series from four heights. To characterize the vertical structure of the flow, we identify 28 current events when the near-bottom (5 mab) along-valley current speed ($|u_b|$) exceeds 0.15 m s^{-1} at site C (Figure 5b, red triangles). There are 8 events with offshore near-bottom flows and 20 events with onshore near-bottom flows. The profiles are further divided into times when the water column was weakly stratified ($\Delta\rho < 0.05$ kg m^{-3}, the estimated accuracy of the density measurements) and times when there is moderate stratification ($\Delta\rho > 0.2$ kg m^{-3}, Figure 5c, dashed lines). (Here $\Delta\rho$ is the density difference between 0.5 and 40 mab.) Subsequently we refer to these events as unstratified and moderately stratified. Periods of stronger stratification ($\Delta\rho > 0.5$ kg m^{-3}) occur from May to October (Figure 7b), but the maximum $\Delta\rho$ during the winter USGS deployment is about 0.4 kg m^{-3} (Figure 5c). All the unstratified (six profiles) and moderately stratified (three onshore and three offshore) along-valley current profiles ($|u_b| > 0.15$ m s^{-1}) and the associated veering of the currents relative to the near-bottom flow are shown in Figure 8. Current profiles when there is intermediate stratification (0.2 kg m$^{-3} > \Delta\rho > 0.05$ kg m^{-3}) typically resemble the moderately stratified profiles.

Unstratified, onshore along-valley flow ($u_b < -0.15$ m s^{-1}, $\Delta\rho < 0.05$ kg m^{-3}) is nearly vertically uniform throughout most of the water column, with only a small (typically less than 5°) veering with height above the bottom (Figure 8a). Thus, when the water column is unstratified, the topographic steering of the flow by the valley extends throughout the entire water column. Unstratified, offshore flow events ($u_b > 0.15$ m s^{-1}, $\Delta\rho < 0.05$ kg m^{-3}) did not occur during the winter USGS deployment.

When stratification is moderate ($\Delta\rho > 0.2$ kg m^{-3}, $u_b < -0.15$ m s^{-1}; Figure 8b), the three onshore along-valley current profiles have a well-defined maximum in the lower half of the water column, with large vertical shear above the maximum, and weaker flow in the upper water column. There is also substantial veering relative to unstratified onshore flow. Relative to the near-bottom onshore along-valley flow, the current
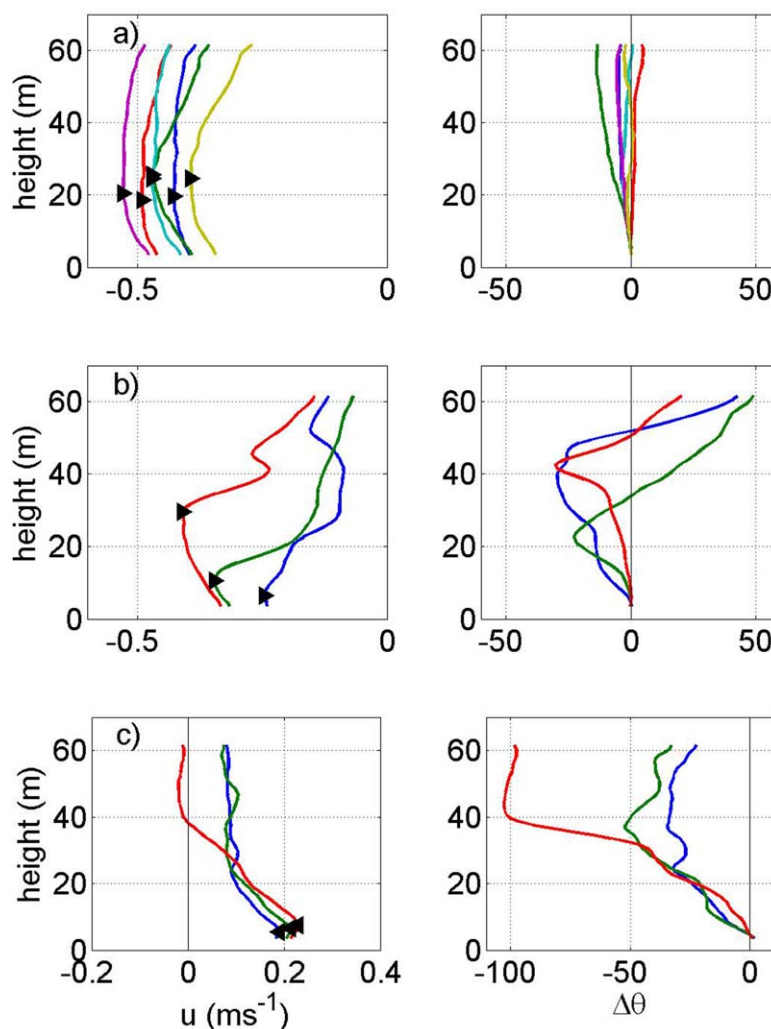
Figure 8. Profiles of (left column) low-passed, along-valley currents and (right column) current orientation relative to the orientation of near-bottom flow $\Delta\theta$ at site C when $|u_b| > 0.15$ m s^{-1} for all (a) unstratified ($\Delta\rho < 0.05$ kg m^{-3}) onshore flow events, (b) moderately stratified ($\Delta\rho > 0.2$ kg m^{-3}) onshore flow events, and (c) moderately stratified offshore flow events. There were no unstratified, offshore flow events with $u_b > 0.15$ m s^{-1}. Positive $\Delta\theta$ is counterclockwise veering. Black triangles identify the height and magnitude of the maximum current (h_{max} and u_{max}, respectively) for each profile. Valley rim is about 20 mab at site C (see Figure 3).

veers 20°–30° clockwise toward an eastward, along-shelf orientation 20–40 mab. Higher up in the water column there is counterclockwise veering possibly associated with the surface Ekman layer. For moderately stratified, onshore flow, the height of the maximum current, the maximum current shear, and where the veering changes from clockwise to counterclockwise vary from one profile to the next.

Moderately stratified, offshore flow ($u_b > 0.15$ m s^{-1}, $\Delta\rho > 0.2$ kg m^{-3}) is maximum approximately 5 mab and then decreases with height above the bottom (Figure 8c). The veering is consistently clockwise with height above the bottom throughout the water column, turning from offshore along-valley near the bottom toward southward along-shelf at middepth. The clockwise veering is typically 20°–30° within the valley (~20 mab) and more variable above the valley rim.

The height of the maximum along-valley current typically decreases with increasing stratification, with one exception (Figure 9). Near-bottom (<20 mab) veering within the valley increases with slight increases in the near-bottom stratification for both onshore and offshore flows (Figure 10). However, onshore flows are consistently associated with relatively weak near-bottom stratification within the valley, while offshore flows are often associated with stronger near-bottom stratification within the valley (Figure 11). Consequently, near-bottom veering is typically larger for offshore flows (Figure 10, red) than for onshore flows (Figure 10, blue).
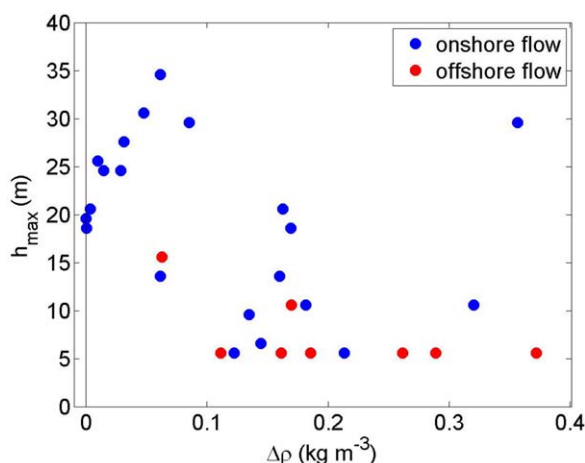
Figure 9. Height of maximum low-passed along-valley current h_{max} as a function of near-bottom density difference $\Delta\rho = \rho(0.5\,\text{mab}) - \rho(40\,\text{mab})$ at site C for the 28 events when $|u_b| > 0.15\,\text{m s}^{-1}$ (Figure 5). Blue circles are onshore along-valley flow events and red circles are offshore along-valley flow events. An estimate of bulk stratification from 0.5 to 68.5 mab was not used because h_{max} did not exceed 40 m and there was often a thin layer of low-salinity water near the surface associated with the Hudson River discharge (Figure 7b).

Maximum along-valley onshore currents reached $-0.6\,\text{m s}^{-1}$ and are correlated with the associated eastward wind stresses (Figures 12a, 5a, and 5b). Maximum offshore currents are about $0.2\,\text{m s}^{-1}$, typically weaker than maximum onshore currents, and do not increase with increasing westward wind stresses; though offshore flow events only occur following westward or near-zero wind stresses. The height of the maximum along-valley current (h_{max}) is less than 10 m for moderate westward wind stresses ($\tau^{sm} < -0.1\,\text{N m}^{-2}$) and is generally greater than 10 m for moderate eastward wind stresses ($\tau^{sm} > 0.1\,\text{N m}^{-2}$) (Figure 12b). The dependence of h_{max} on both the wind stress (Figure 12b) and stratification (Figure 9) suggests that using observations from a single height (for example, 5 mab as in section 3) may be misleading in characterizing the overall flow structure and the along-valley transport.

4.2. Along-Valley Transport

There is a difference in the response to eastward and westward wind stresses of both the height (Figure 12b) and speed (Figure 12a) of the maximum currents and the vertical structure of the along-valley flows (compare Figure 8b and Figure 8c). This suggests there may be a corresponding difference in the along-valley transport response to eastward and westward wind stresses. To determine if this is the case, time series of along-valley transport U were estimated for the winter and spring USGS ADCP deployments within the valley by integrating the along-valley flow from the bottom up to the first zero-crossing in the subtidal current profile or the surface if the along-valley current was unidirectional. Along-valley transports were also estimated for three MESA sites (M13, M14, and M16) for which there were current observations at three or more depths. In all cases, the valley is assumed to be 5 km wide and the along-valley current is assumed
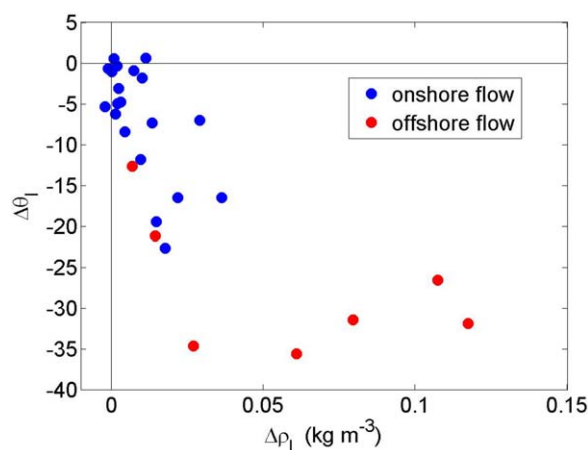

Figure 10. Veering of near-bottom flow $\Delta\theta_l$ between 4.5 mab (near the bottom) and 21.5 mab (near height of valley rim) as a function of the density difference $\Delta\rho_l$ between 0.5 and 10 mab at site C. Positive veering is counterclockwise.

to be uniform across the width of the valley. Uncertainties in the transport estimates from the MESA study are larger than for the USGS study because of the sparser vertical coverage and the less accurate current meters. Nevertheless, the two data sets yield a similar dependence of along-valley transport on wind stress (Figure 13).

Correlations between the transport time series from different USGS sites within the valley exceed 0.85 for all site pairs during both the winter and spring deployments. The corresponding regression coefficients are 1.0 to the accuracy of the estimates, except at site A, where the transport is about half the size of the transport estimates at the other sites (B, C, F, and G). This suggests that roughly half of the convergence in the
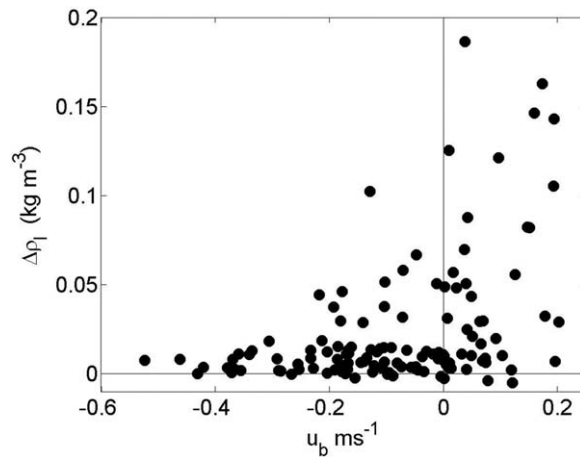
Figure 11. Daily values of the density difference $\Delta\rho_l = \rho(0.5\text{mab}) - \rho(10$ mab) within the valley versus daily values of the low-passed near-bottom along-valley current u_b at 5 mab at site C for December 1999 to April 2000. Positive currents are offshore.

along-valley transport occurs between sites A and B, with the remaining half between site A and the coast. This implies that the upwelling/downwelling associated with the transport convergence is concentrated where the seafloor rises rapidly from site B to the head of the valley (Figure 3).

Daily values of the subtidal along-valley transport exhibit a linear dependence on wind stress in the range -0.1 N m$^{-2} < \tau^{sm}$ < 0.3 N m^{-2} (Figure 13). In this wind stress range, the correlations are about 0.8 near the head of the valley at sites A and B (0.6 at M13) and decrease slightly with distance offshore to about 0.7 at sites F and M16. The regression slope is about 0.4×10^6 m^3 s^{-1}/N m^{-2}. Thus for wind stress magnitudes of less than 0.1 N m^{-2} the transport response to eastward and westward winds is symmetric. While there are relatively few westward wind stresses between -0.1 and -0.5 N m^{-2}, the associated transports are consistently at or below the 0.4×10^6 m^3 s^{-1}/N m^{-2} regression slope (dashed line, Figure 13). This is in contrast to transports associated with eastward wind stresses between 0.1 and 0.5 N m^{-2} that are evenly distributed above and below the regression slo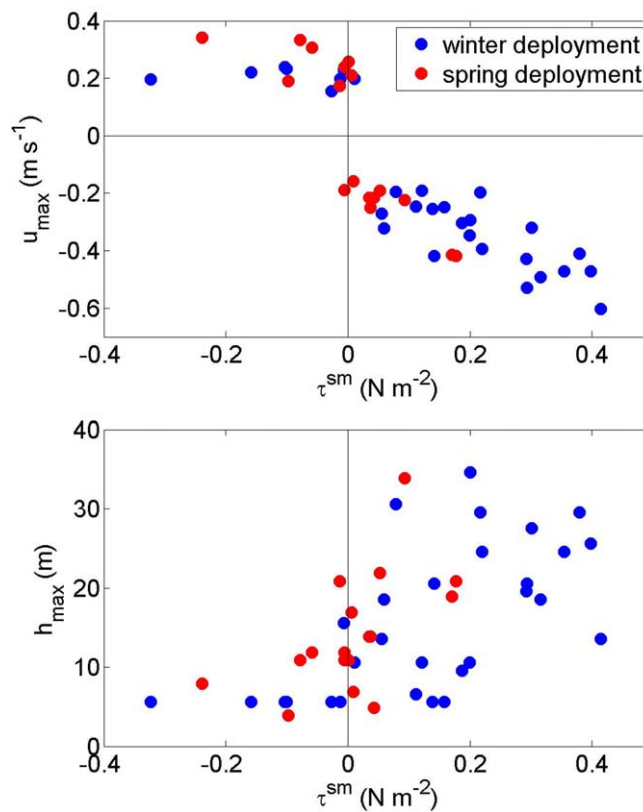pe. This suggests there is an asymmetry in the transport response to eastward and westward wind stresses with magnitudes exceeding 0.1 N m^{-2}. (Note that the USGS transport estimates are typically smaller than the MESA estimates for westward wind stress between -0.1 and -0.5 N m^{-2}. We suspect this is because the sparse vertical coverage of the MESA current measurements relative to the USGS ADCPs (Figure 3) does not accurately resolve the vertical structure of the thin near-bottom enhanced flow during westward winds (Figure 8c)). The response of along-valley transport to the along-valley pressure gradient during the winter USGS deployment is similar to the wind stress response. The along-valley transport in response to the Groundhog Day Gale 2 February 1976 when wind stress exceeded 1 N m^{-2} was about -0.17×10^6 m^3 s^{-1} at sites M14 and M16, about the same as the transport for a wind stress of 0.3 N m^{-2}. While the Groundhog Day Gale is only a single event, this suggests that the along-valley

Figure 12. (a) Maximum low-passed along-valley current (u_{max}) and (b) height of maximum current h_{max} (Figure 8) as a function of low-passed wind stress τ^{sm} (orientation 110°T, leading u_{max} by 10 h) for 28 current events ($|u_b| > 0.15$ ms^{-1}) during the winter (blue, December 1999 to April 2000; Figure 5b) and 16 current events during the spring (red, April to June 2006) USGS deployments.
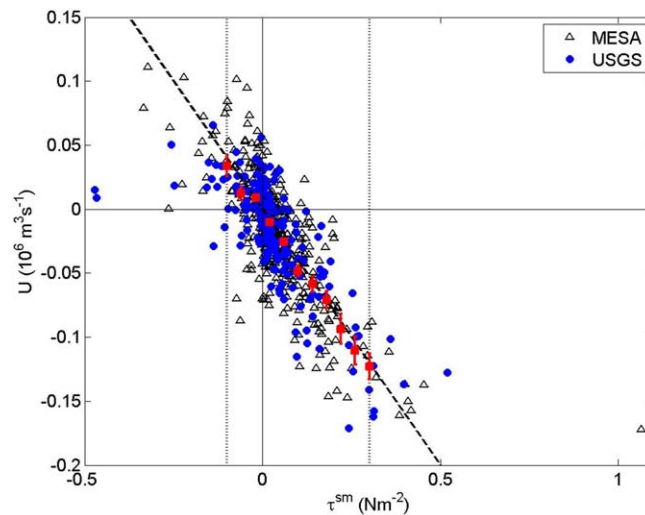
Figure 13. Daily values of the low-pass filtered along-valley transport U (sites C, G, and M14) as a function of the wind stress τ^{sm} (orientation 110° and leading transport by 10 h; Gaps in the M14 transport time series were filled with data from sites M13 and M16). Red squares are bin averages with standard error bars (standard deviation divided by the square root of the number of daily samples in the bin average). The transport is a roughly linear function of wind stress (dashed line with regression slope of 0.4×10^6 m³ s⁻¹/N m⁻²) between the vertical dotted lines -0.1 Nm⁻² $< \tau^{sm} < 0.3$ Nm⁻². The event when $\tau^{sm} > 1$ N m⁻² was the Groundhog Day Gale 2 February 1976.

transport response may be limited during extreme events. While larger transports tend to occur in winter, when there are stronger wind stresses, there is not an obvious difference in the relationship between wind stress and transport between summer and winter (not shown).

4.3. The Along-Valley Momentum Balance

To determine the dynamics of the flow in Hudson Shelf Valley, we initially focus on the depth-average along-valley momentum equation to determine the dominant balance of terms and to evaluate whether the estimates are accurate enough to roughly close the momentum balance. The vertically integrated momentum balance integrated along the valley from site B ($x = x_B$) to site F ($x = x_F$) may be written as (see Appendix A)

$$\frac{\partial}{\partial t} \int_{x_B}^{x_F} \hat{u}\,dx + \hat{u}^2 \Big|_{x_B}^{x_F} + \frac{\partial}{\partial y} \int_{x_B}^{x_F} \hat{u}\hat{v}\,dx - f \int_{x_B}^{x_F} \hat{v}\,dx = -\frac{P_b}{\rho_o}\Big|_{x_B}^{x_F} - \int_{x_B}^{x_F} \frac{D}{\rho_o \tilde{D}} \frac{\partial P'_b}{\partial x}\,dx - \frac{\rho \hat{g} z}{\rho_o}\Big|_{x_B}^{x_F} + \int_{x_B}^{x_F} \frac{(\tau^{sx} - \tau^{bx})}{\rho_o \tilde{D}}\,dx \quad (1)$$

where,

$$\hat{u} = \frac{1}{D} \int_{-D}^{\eta} u\,dz \text{ and } \tilde{D} = \frac{1}{(x_F - x_B)} \int_{x_B}^{x_F} D\,dx,$$

$z = 0$ at the mean surface and is positive upward, D is the water depth, and $P'_B(x)$ is the deviation of the bottom pressure from a linear pressure difference between sites B and F. All of the terms in (1) can be estimated from the observations (see Appendix A) except the cross-valley gradient in the momentum flux (third term on the left-hand side of equation (1)) and the form drag associated with correlations between variations in the along-valley bottom pressure gradient and water depth (second term on the right-hand side of equation (1)). To be consistent with subsequent analysis, the evaluation focuses on the 28 current events noted in Figure 5b. The following analysis focuses on along-valley momentum balance at subtidal time scales—the subtidal cross-valley momentum balance which is geostrophic and the momentum balance at tidal time scales are briefly discussed in Appendix A.

The along-valley pressure difference has the largest standard deviation (Table 1). The standard deviation of the Coriolis term is about 40% of the pressure difference, the wind stress is about 20%, and the buoyancy force is 15%. The standard deviations of the remaining terms are 10% or less of the pressure difference term. The correlation between the pressure difference and the sum of the other terms is 0.94. The regression slope is 0.60 ± 0.09 suggesting either the terms that were not estimated are important, or the pressure gradient estimate is too large, or estimates of the other terms are too small (see section 5.2). Results are similar if the entire subtidal time series is considered, rather than the 28 events in Figure 5b; the correlation between the pressure difference and the sum of the other terms is 0.88 and regression slope is 0.56 ± 0.07.

To examine what controls the vertical structure of the flow (Figure 8), examples of the vertical structure of the along-valley pressure gradient and the Coriolis term are shown in Figure 14 for unstratified onshore flow, stratified onshore flow and stratified offshore flow. The pressure gradient is approximately barotropic, that is, nearly uniform with depth. In the middle of the water column, there is a clear tendency for the

Table 1. Standard Deviation of Terms in the Subtidal Along-Valley Momentum Balance (2) in Different Regions of the Water Column for the 28 Current Events With Along-Valley Velocities in Excess of 0.15 m s^{-1} at USGS Site C (Figure 5)[a]

Term	Depth-Average	Upper Layer	Lower Layer
$\partial \hat{u}/\partial t$	1.0	0.6	0.4
$\Delta \hat{u}^2$	0.6	1.3	1.3
$f\hat{v}$	4.2	4.7	2.0
ΔP_b	10.7	10.7	10.7
$\Delta \rho \hat{g} z$	1.5	1.3	0.3
$\tau^{sx}/\bar{D}$	2.3	3.3	
$\tau^{bx}/\bar{D}$	1.1		5.7

[a]Units are 10^{-6} m s^{-2}. See Appendix A for how each term is calculated. Lower layer is defined as the water column below the along-valley velocity maximum; upper layer, which includes the surface Ekman layer, is the water column above the velocity maximum (see Figure 8, triangles).
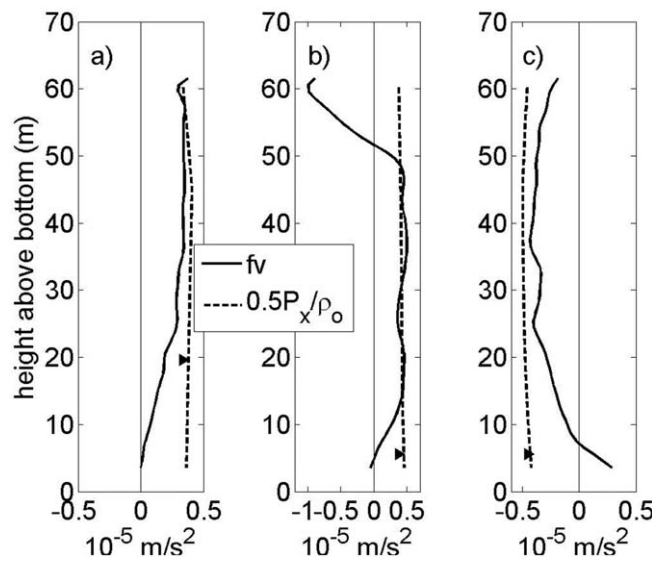

Figure 14. Examples of vertical profiles of the dominant terms in the along-valley momentum balance, the Coriolis and the pressure gradient for (a) an unstratified onshore flow event, (b) a stratified onshore flow event, and (c) a stratified offshore flow event. The pressure gradient is divided by 2. The triangle marks the height of maximum along-valley current (Figure 8).

Figure 15. Schematic of the different dynamical regions associated with the along-valley current profiles.

Coriolis term to be approximately half the pressure gradient (similar to the depth-average momentum balance), Potential reasons for the difference in magnitude between the pressure gradient and Coriolis term are discussed in section 5.2. This relationship holds at middepth for all but one of the 28 events (Figure 16b, blue circles). The exception is the event having the largest magnitude wind stress and along-valley pressure gradient. We surmise turbulent stresses extend throughout the water column and hence there is not a geostrophic interior during this event. The Coriolis and the pressure gradient term (divided by 2) do not balance near the bottom and near the surface where presumably turbulent stresses are large.

Since we do not have observations of the turbulent stress profiles, to further investigate the dynamics the water column is divided into two distinct dynamical regions, a turbulent bottom boundary layer and a geostrophic interior (Figure 15). We assume that the transition between these two regions is at $z=-D+h_{max}$ the depth of the maximum along-valley current (Figures 8 and 14, black triangles). This follows from assuming the turbulent stress can be represented as $\tau^x(z) \approx \rho K \partial u/\partial z$, where K is an eddy viscosity. Then since $\partial u/\partial z=0$ at $z=-D+h_{max}$ this implies $\tau^x(z=-D+h_{max}) \approx 0$.
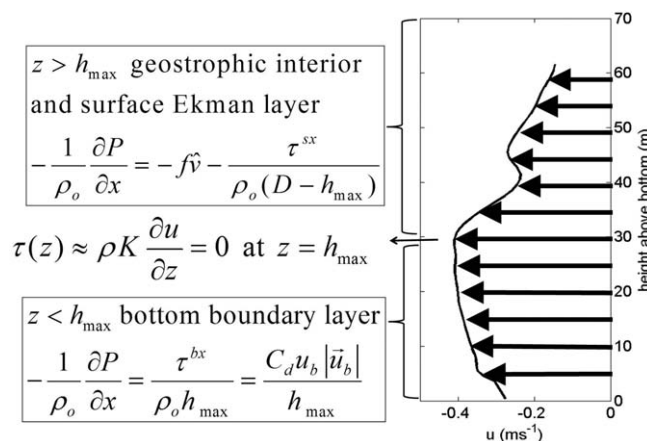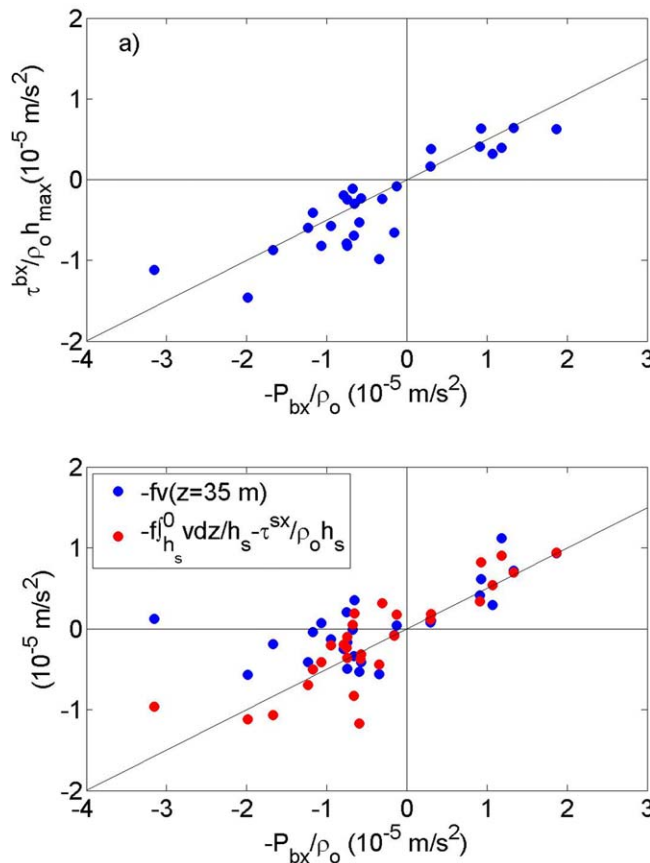
Figure 16. Comparisons of the along-valley pressure gradient term to (a) the bottom stress term in the bottom boundary layer ($z < -D + h_{max}$) and (b) the Coriolis at mid-depth (blue) and the Coriolis plus wind stress terms in the combined interior and surface boundary layer ($0 > z > -D + h_{max}$) (red) for all 28 along-valley current events ($|u_b| > 0.15 \text{ms}^{-1}$).

Integrating the along-valley momentum balance from the bottom ($z = -D$) to $z = -D + h_{max}$ and dividing by h_{max} yields

$$\frac{\partial}{\partial t}\int_{x_B}^{x_F}\hat{u}dx + \hat{u}^2\Big|_{x_B}^{x_F} - f\int_{x_B}^{x_F}\hat{v}dx$$
$$= -\frac{P_b}{\rho_o}\Big|_{x_B}^{x_F} - \frac{\rho\hat{g}z}{\rho_o}\Big|_{x_B}^{x_F} - \int_{x_B}^{x_F}\frac{\tau^{bx}}{\rho_o h_{max}}dx, \tag{2}$$

where the depth-averages are over the lower layer. Note (2) excludes terms that could not be estimated: the cross-valley nonlinear momentum flux, the form drag, and the vertical flux of momentum through $z = -D + h_{max}$. The dominant balance in (2) is between the along-valley pressure difference and the bottom stress; the other terms that could be estimated are relatively small (Table 1). The correlation between the pressure difference and bottom stress terms is 0.87 and the regression slope is 0.46 ± 0.10 (Figure 16a). Note the Coriolis force normally associated with a bottom Ekman layer is small (20% of the pressure difference) because the valley bathymetry inhibits the current veering and development of a cross-valley flow.

Integrating the along-valley momentum balance from the surface ($z = 0$) to $z = -h_s$, where $h_s = D - h_{max}$ is the thickness of the upper layer, yields

$$\frac{\partial}{\partial t}\int_{x_B}^{x_F}\hat{u}dx + \hat{u}^2\Big|_{x_B}^{x_F} - f\int_{x_B}^{x_F}\hat{v}dx = -\frac{P_b}{\rho_o}\Big|_{x_B}^{x_F} - \frac{\rho\hat{g}z}{\rho_o}\Big|_{x_B}^{x_F} + \int_{x_B}^{x_F}\frac{\tau^{sx}}{\rho_o h_s}dx, \tag{3}$$

where the depth-averages are over the upper layer and terms that could not be estimated are not included. The dominant terms in (3) are the along-valley pressure difference, the Coriolis term, and the wind stress; the other terms that could be estimated are relatively small (Table 1). This is consistent with the upper layer consisting of a combination of a geostrophic interior and a surface Ekman layer. The correlation between the pressure difference and the sum of the Coriolis and wind stress terms is 0.86 and the regression slope is 0.48 ± 0.11 (Figure 16b, red circles).

The observed momentum balances indicate that at midshelf site C in Hudson Shelf Valley during the winter the strength of the along-shelf flow is limited by bottom stress, not by the development of an along-valley density gradient that opposes the barotropic pressure gradient [e.g., *She and Klinck*, 2000] nor by the nonlinear acceleration term $u\partial u/\partial x$ [*Freeland and Denman*, 1982]. However, both these terms may be important near the head of Hudson Shelf Valley where there are more substantial along-valley variations in transport and depth, and stronger lateral and vertical density gradients. It is also possible that along-valley density

gradients are more important to the midshelf valley dynamics in summer when there is stronger stratification. However, current profiles at site G (near site C Figure 3) in spring, when the stratification is stronger than during the winter (Figure 7b), exhibit the same vertical structure and asymmetry seen in Figures 8b and 8c.

Based on the observed dynamical balances, a quantitative relationship of the wind-driven portion of the along-valley current can be constructed as follows. Assume that the depth-average along-shelf flow (v^{sh}) east or south of the valley is proportional to the along-shelf wind stress, $v^{sh} \sim a\tau^{sm}$ [e.g., *Beardsley et al.*, 1985; *Shearman and Lentz*, 2003] and that the depth-average along-shelf flow is in geostrophic balance, $\rho_o f v^{sh} = \partial P / \partial x$ [e.g., *Shearman and Lentz*, 2003]. Assuming in the bottom boundary layer within the valley that $h_{max} \partial P / \partial x \approx -\rho_o C_{dmx} u_{max} |u_{max}|$ yields

$$u_{max} \approx -sign\left(\frac{\partial P}{\partial x}\right)\left(\frac{h_{max}}{C_{dmx}\rho_o}\frac{\partial P}{\partial x}\right)^{\frac{1}{2}} \approx -sign(\tau^{sm})\left(\frac{af\tau^{sm}h_{max}}{C_{dmx}}\right)^{\frac{1}{2}}, \qquad (4)$$

where f is the Coriolis parameter and C_{dmx} is a drag coefficient based on the maximum along-valley current.

Equation (4) implies the maximum along-valley flow depends on the wind stress and the thickness of the bottom boundary layer (h_{max}). The thickness of the bottom boundary layer, in turn, depends on the near-bottom stratification (Figure 9) and hence on the direction of the along-valley flow (Figure 11) and the wind stress (Figure 12b). When the water column is unstratified, the bottom boundary is thick and along-valley flow is relatively strong (Figure 8a). Stratification limits the thickness of the bottom boundary layer and, hence, the maximum along-valley flow. This may also account for the difference between the onshore and offshore flow response in the valley (Figures 8b and 8c). Offshore flow in the valley enhances the near-bottom stratification (Figure 11) resulting in a thinner bottom boundary layer and weaker maximum along-valley flow. Onshore flow reduces the near-bottom stratification resulting in a thicker bottom boundary layer and stronger along-valley flows.

5. Discussion

5.1. Near-Bottom Stratification

An important, unresolved question is why the near-bottom stratification is weaker for onshore along-valley flow than for offshore along-valley flow as seen in Figure 11. We hypothesize that this is due to the near-bottom current shear acting on the along-valley density gradient as shown schematically in Figure 17. During most of the winter deployment there is denser water at site C relative to site B throughout the water column, that is, density increases offshore. During offshore flow, the near-bottom shear strains the along-valley density gradient enhancing the near-bottom stratification. During onshore flow the straining due to the near-bottom shear will reduce the near-bottom stratification. This pattern is consistent with the observed relationship between near-bottom currents and stratification (Figure 11). In this manner, the shelf valley behaves somewhat similar to estuaries where ebbing flow conditions are associated with increased stratification relative to flooding conditions [i.e., *Scully and Friedrichs*, 2007; *Scully et al.*, 2005]. Unfortunately, the few moored density time series are insufficient to determine the vertical and along-valley structure of the density field during onshore and offshore along-valley flow. More detailed observations of the density structure are needed to determine whether this qualitative explanation is correct and how the stratification and along-valley density gradient vary on synoptic and seasonal time scales.

5.2. Along-Valley Momentum Balance

The regression slope between the along-valley pressure gradient and other terms in the along-valley momentum balance is about 0.5, significantly less than 1.0, for the bottom boundary layer, the upper water column and the depth-average (Figure 16). Since different terms are important in the bottom boundary layer and the upper water column, it seems unlikely that this is due to, for example, the bottom drag coefficient being off by a factor of two. It also seems unlikely that the pressure difference between sites B and F is off by a factor of two. Estimates of the along-valley pressure gradient using an empirical-orthogonal-function (EOF) analysis of the pressure time series at sites A, B, C, F or different site pairs yield essentially the same estimates as the finite difference between sites B and F. Consequently, we suspect that one of the
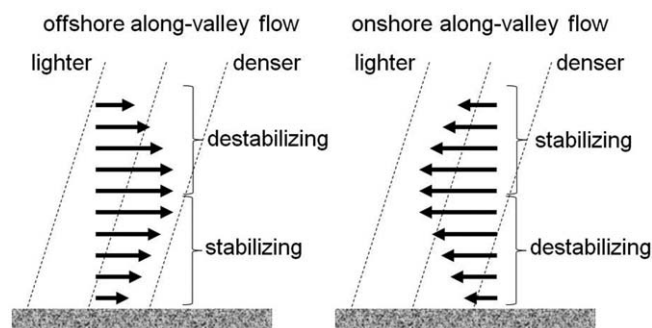
Figure 17. Schematic of how near-bottom shear may enhance near-bottom stratification (stabilizing) for offshore flow or reduce near-bottom stratification (destabilizing) for onshore flow given increasing density with distance offshore.

terms that could not be estimated is large (standard deviation about half the observed pressure difference) and correlated with the pressure difference. Two possibilities are discussed next.

The rough bathymetry along the valley floor (Figure 3) suggests there could be substantial perturbations in the along-valley pressure gradient on scales shorter than the mooring spacing associated with flow separation. This suggests that form drag, correlations between the bathymetric and along-valley pressure gradient variations (second term right-hand side of equation (1)), could be substantial. Assuming the pressure gradient perturbations are barotropic, this term would contribute to both the upper and bottom boundary layer momentum balances. The form drag would have to be similar in magnitude to the bottom stress term to account for the observed discrepancy between the pressure difference and the sum of the other estimated terms in the along-valley momentum balances.

The momentum flux due to $v\partial u/\partial y$, the cross-valley advection of cross-valley gradients in the along-valley flow, may be substantial given that cross-shelf (along-valley) currents in the valley are much faster than those over the adjacent shelf. Accurate estimates of this term are difficult, however, given the large across-valley variations in the bathymetry and the potential for variations in the flow on scales that are short compared to the mooring separations (22 km between sites D and E). Various estimates of this term using the observations at sites D, B, and E near the head of the valley (Appendix A) all have standard deviations of approximately 10^{-6} m s^{-2}, a factor of 10 smaller than the along-valley pressure gradient term (Table 1). This suggests the flow would need to vary substantially on cross-valley scales of order 1 km or less for the $v\partial u/\partial y$ term to be substantial which is certainly plausible. To resolve this would require accurate estimates of the cross-valley variations in the flow, either from observations with much higher cross-valley spatial resolution or from numerical simulations.

5.3. Relationship to Previous Studies of Submarine Canyons

While topographic steering of the flow in Hudson Shelf Valley is qualitatively similar to that seen in other submarine valleys or canyons, characteristics of the currents and dynamics differ substantially from most of the previous studies that have focused on deeper canyons that incise continental slopes [e.g., *Allen and de Madron*, 2009]. Since Hudson Shelf Valley is in shallow water over the continental shelf and it extends nearly to the coast, it experiences a wider range of stratification and the bottom boundary layer plays a more fundamental role in the dynamics compared to larger canyons in deeper water. In particular, the vertical scale of the flow in Hudson Shelf Valley is set by the height of the bottom boundary layer, rather than the vertical scale for a stratified flow (fW/N) related to the Burger number, where W is a canyon width scale and N is the buoyancy frequency [*Kampf*, 2007; *Allen and Hickey*, 2010]. The scale height fW/N is not correlated with the observed h_{max}.

Several scalings have been proposed for the upwelling transport in deep canyons incising continental slopes [*Mirshak and Allen*, 2005; *Kampf*, 2007; *Allen and Hickey*, 2010]. While the scales differ substantially [see *Kampf*, 2007; *Allen and Hickey*, 2010], they depend on a power law where the along-slope current is raised to the 8/3 [*Mirshak and Allen*, 2005], squared [*Kampf*, 2007], or cubed [*Allen and Hickey*, 2010]. The relationship between wind stress and along-valley transport in Hudson Shelf Valley is linear for moderate wind stresses (Figure 13). This suggests a linear relationship between along-valley transport and the upstream along-shelf current since previous studies have found a linear relationship between wind stress and along-shelf flow in the Middle Atlantic Bight [*Beardsley et al.*, 1985; *Shearman and Lentz*, 2003]. USGS sites D and E are probably too close to Hudson Shelf Valley to directly test this relationship. However,
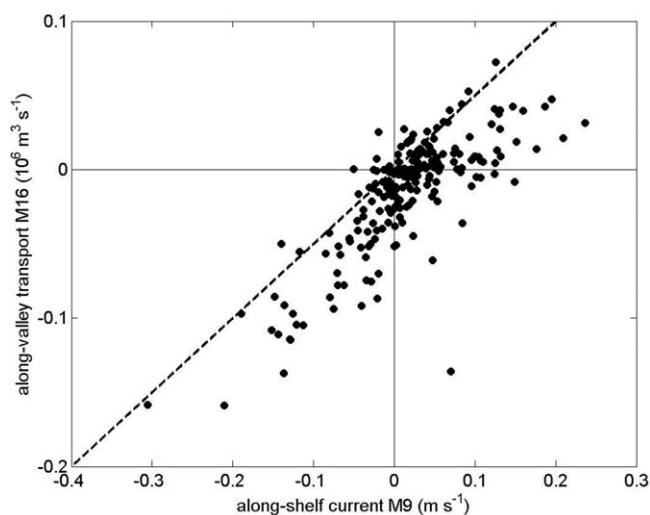
Figure 18. Daily values of the along-valley transport at MESA site M16 versus the along-shelf current 8 mab at site M9. Dashed line has a slope of $0.5 \times 10^6 (m^3 \ s^{-1})/(m \ s^{-1})$.

comparisons between the MESA sites M9 on the shelf and M16 in the valley (see Figure 4) do suggest a linear relationship (Figure 18).

Finally, the difference in the vertical structure of onshore/offshore along-valley current profiles (Figure 8) in Hudson Shelf Valley is associated with differences in the stratification within the valley and the resulting impact on the thickness of the bottom boundary layer. Specifically, stronger stratification during offshore currents results in a thinner bottom boundary and weaker along-valley currents. This is fundamentally different from the inviscid asymmetry to upwelling and downwelling-favorable along-shelf flows found by *Klinck* [1996] and others.

6. Summary

Observations in Hudson Shelf Valley during two USGS studies (winter 1999–2000 and spring 2006), the MESA project (1974–1978), and a NMFS study (1987–1989) indicate that along-valley near-bottom currents are highly correlated with the east-west component of wind stress for events having time scales of days (Figures 5 and 6). Eastward wind stress causes a setdown of sea level at the coast and the resulting cross-shelf (along-valley) pressure gradient drives an onshore near-bottom flow in the valley (Figure 5). Westward wind stress causes a sea level setup and an offshore near-bottom flow in the valley. Associated onshore along-valley transport (Figure 13) can be 20–30% of the along-shelf transport [*Lentz*, 2008a]. The relationship between wind stress and along-valley flow combined with the annual cycle in the wind forcing results in an annual cycle in the near-bottom along-valley flow with monthly mean onshore flows of ~0.1 m s^{-1} in winter and near zero in summer (Figure 7a).

The vertical structure of the currents depends on both the stratification and the direction of the along-valley flow. During unstratified conditions and strong (>0.15 m s^{-1}) along-valley onshore currents, topographic steering extends to near the surface, and the velocity profiles are nearly vertically uniform (Figure 8a). During stratified conditions, the along-valley velocity profiles are vertically sheared and reach a maximum at some height (h_{max}) above the bottom. During onshore currents, h_{max} tends to be smaller for stronger stratification, whereas during offshore currents h_{max} remains near the bottom (~5 mab; Figure 9). Above h_{max}, the along-valley flow decreases and the current rotates clockwise (Figures 8b and 8c).

Estimates of the terms in the along-valley momentum balance indicate that within the bottom boundary layer, the dominant balance is between bottom stress and the along-valley pressure gradient (Figure 16a). The v-shaped valley bathymetry inhibits development of a bottom Ekman layer. Consequently, the magnitude of the bottom stress, and hence the magnitude of the near-bottom along-valley flow, is set by the along-valley pressure gradient (which is in turn set by the wind stress) and the height of the bottom boundary layer, which depends on the stratification. Above the bottom boundary layer, the flow turns toward an along-shelf (cross-valley flow) so that the along-valley pressure gradient is balanced by Coriolis—an interior geostrophic balance, and the wind stress—a surface boundary layer Ekman balance (Figure 16b). In both the bottom boundary layer and the upper water column, the pressure gradient term exceeds the sum of the other estimated terms suggesting the importance of either form drag or cross-valley momentum fluxes that could not be estimated.

Along-valley density gradients do not substantially contribute to the along-valley pressure gradient in the winter observations. However, we hypothesize that straining of the along-valley density gradient causes the

observed tendency for offshore near-bottom flow driven by westward wind stress to increase the near-bottom stratification within the valley relative to onshore flow driven by eastward wind stress (Figure 11). As a consequence, the bottom boundary layer is thinner, maximum along-valley flow is closer to the bottom and often weaker for westward wind stress (offshore flow) than for eastward wind stress (onshore flow; Figures 8, 9, 10, and12). Consequently, onshore along-valley transport driven by an eastward wind stress greater than 0.1 N m^{-2} often exceeds offshore transport driven by a westward wind stress of the same magnitude (Figure 13).

Appendix A: Estimation of Terms in the Along-Valley Momentum Balance

The vertically integrated along-valley momentum balance is

$$\frac{\partial}{\partial t}\int_{-h}^{\eta}u\,dz+\frac{\partial}{\partial x}\int_{-h}^{\eta}u^2\,dz+\frac{\partial}{\partial y}\int_{-h}^{\eta}uv\,dz-f\int_{-h}^{\eta}v\,dz=-\frac{h}{\rho_o}\frac{\partial P_b}{\partial x}-\frac{\partial}{\partial x}\int_{-h}^{\eta}\frac{\rho gz}{\rho_o}\,dz+\frac{\tau^{sx}}{\rho_o}-\frac{\tau^{bx}}{\rho_o}, \qquad (A1)$$

where x,y,z are the along-valley (positive offshore), cross-valley, and vertical (positive upward) coordinates, u,v,w are the corresponding velocities, η is the sea surface variation, h is the water depth relative to the mean sea level, $f=0.94\times10^{-4}$ s^{-1} is the Coriolis frequency, P_b is the bottom pressure, ρ is the density, τ^{sx} is the along-valley wind stress, and τ^{bx} is the along-valley bottom stress. Integrating (A1) along the valley from site B $(x=x_B)$ to site F $(x=x_F)$ and dividing by the average water depth between sites B and F $(\tilde{D})$ yields the along-valley momentum balance given in (1) (section 4.3). All of the terms in (1) can be estimated using the USGS winter instrument array observations except the cross-valley gradient in the momentum flux (third term on the left-hand side) and the form drag associated with correlations between the along-valley gradient in bottom pressure gradient variations and water depth variations (second term on the right-hand side). Terms are estimated using hourly samples and subsequently low-pass filtered to focus on subtidal variability. Vertical integrals are estimated using a trapezoidal rule and assuming no vertical variations to extrapolate to the surface and bottom. Terms involving integrals in x are approximated as weighted sums of the estimates from sites B, C, and F (weights 0.25, 0.5, 0.25). The average water depth between sites B and F $(\tilde{D})$ is estimated using the USGS bathymetry shown in Figure 3.

The temporal acceleration term is estimated as a centered difference over 2 h at each bin height of the ADCP current profiles. The along-valley advective flux and the bottom pressure difference terms are estimated as differences between the observations at sites B and F. The density term is estimated using sites B and C and assuming a constant gradient because there were not density measurements spanning the water column at site F. The surface stress τ^{sx} is estimated using wind observations from NDBC buoy 44025 and a neutral bulk formula [*Fairall et al.*, 2003]. The wind stress is assumed to be spatially uniform over the study area. The bottom stress is estimated assuming a quadratic drag law, $\tau^{bx}=\rho C_D u_b|\vec{u}_b|$, with $C_D=0.85\times10^{-3}$ for u_b at 5 mab. This drag coefficient was determined from direct covariance stress estimates and log-profile estimates of bottom stress at sites A and B. It is also consistent with the roughness estimate $z_o=5\times10^{-6}$ m determined by *Harris et al.* [2003] by comparison between a wave-current interaction model to estimate bed shear stress [*Wiberg et al.*, 1994] and the USGS observations at site A. This estimate of the drag coefficient is the same as a direct covariance stress estimate from the New England shelf [*Shaw et al.*, 2001] and smaller than an estimate for the southern flank of Georges Bank ($C_D=1.2\times10^{-3}$ for u_b at 5 mab) [*Werner et al.*, 2003; see also *Lentz*, 2008a, Appendix B].

A rough estimate of the nonlinear cross-valley momentum flux term (third term left-hand side of Equation (A1)) is made using the current observations from sites D, B, and E. The current observations from sites D and E are used to make a finite difference estimate of $\partial u/\partial y$ centered on site B with v from site B. The 22 km separation between sites D and E greatly exceeds the width of the valley suggesting this is not a well-resolved estimate. Estimates based on just sites D and B, just sites B and E, and using a forward differencing depending on the direction of the flow all have similar magnitudes to the finite difference based on measurements from D and E.

The subtidal depth-averaged along-valley momentum balance is discussed in section 4.3. At tidal time scales the dominant terms in the along-valley momentum balance are the temporal acceleration and the

pressure gradient. Time series of the along-valley pressure gradient are well correlated with the sum of the other terms in the along-valley momentum balance for both tidal and subtidal variability. Correlations are 0.88 in both cases, with regression slopes of 0.56 for the subtidal variability and 0.75 for tidal variability.

The focus here is on the along-valley momentum balance (1) because this describes the forcing of the along-valley flow. However, for completeness, the cross-valley momentum balance

$$\frac{\partial \hat{v}}{\partial t} + \frac{1}{D}\frac{\partial(\hat{u}vD)}{\partial x} + \frac{1}{D}\frac{\partial(\hat{v^2}D)}{\partial y} + f\hat{u} = -\frac{1}{\rho_o}\frac{\partial P^b}{\partial y} - \frac{1}{\rho_o D}\frac{\partial(\rho \hat{g}zD)}{\partial y} + \frac{\tau^{sy}}{\rho_o D} - \frac{\tau^{by}}{\rho_o D} \qquad (A2)$$

is also examined. Terms in the cross-valley momentum balance are estimated centered at site B, using the observations at sites D and E to estimate the depth-average cross-valley gradients and following the methods outlined above for the along-shelf momentum balance. The cross-valley gradient estimates are over the separation between sites D and E, 22 km, much larger than the width of the valley ∼5 km, so they may not be representative of the pressure gradient within the valley. At subtidal time scales, standard deviations of the cross-valley pressure gradient and the Coriolis force associated with the strong along-valley flow exceed the other terms by an order of magnitude. The correlation between $-\partial P^b/\partial y$ and $f\hat{u}$ is 0.65 and the regression slope is ∼1, indicating a geostrophic balance.

References

Allen, S. E. (1996), Topographically generated, subinertial flows within a finite length canyon, *J. Phys. Oceanogr.*, *26*, 1608–1632.

Allen, S. E., and X. D. de Madron (2009), A review of the role of submarine canyons in deep-ocean exchange with the shelf, *Ocean Sci.*, *5*, 607–620.

Allen, S. E., and B. M. Hickey (2010), Dynamics of advection-driven upwelling over a shelf break submarine canyon, *J. Geophys. Res.*, *115*, C08018, doi:10.1029/2009JC005731.

Beardsley, R. C., W. C. Boicourt, L. C. Huff, J. R. McCullough, and J. Scott (1981), CMICE: A near-surface current meter intercomparison experiment, *Deep-Sea Res.*, *28A*, 1577–1603.

Beardsley, R. C., and W. C. Boicourt (1981), On estuarine and continental-shelf circulation in the Middle Atlantic Bight, in *Evolution of Physical Oceanography*, edited by B. A. Warren and C. Wunsch, pp. 198–233, MIT Press, Cambridge, Mass.

Beardsley, R. C., D. C. Chapman, K. H. Brink, S. Ramp, and R. Schlitz (1985), The Nantucket Shoals Flux Experiment: Part I. A basic description of the current and temperature variability, *J. Phys. Oceanogr.*, *15*, 713–748.

Bigelow, H. B. (1933), Studies of the waters on the continental shelf, Cape Cod to Chesapeake Bay. I. The cycle of temperature, *Pap. Phys. Oceanogr. Meteorol.*, *2*, 1–135.

Boyer, D. L., D. B. Haidvogel, and N. Perenne (2004), Laboratory-numerical model comparisons of canyon flows: A parameter study, *J. Phys. Oceanogr.*, *34*, 1588–1609.

Boyer, D. L., J. Sommeria, A. S. Mitrovic, V. K. C. Pakala, S. A. Smirnov, and D. ETLING (2006), Effects of boundary turbulence on canyon flows forced by periodic along-shelf currents, *J. Phys. Oceanogr.*, *36*, 813–826.

Butman, B., P. S. Alexander, C. K. Harris, F. S. Lightsom, M. A. Martini, M. B. ten Brink, and P. A. Traykovski (2003a), Oceanographic observations in the Hudson Shelf Valley, December 1999-April 2000: Data Report, *U.S. Geol. Surv. Open File Rep.*, 02–217, Coastal and Marine Geology Program, Woods Hole Field Center, Woods Hole, Mass., [DVD-ROM]. [Available at http://pubs.usgs.gov/of/2002/of02-217/.]

Butman, B., T. J. Middleton, E. R. Thieler, and W. C. Schwab (2003b), Topography, shaded relief and backscatter intensity of the Hudson Shelf Valley, Offshore of New York, U.S. Geol. Surv. Open File Rep., 03–372, Coastal and Marine Geology Program, Woods Hole Field Center, Woods Hole, Mass. [Available at http://pubs.usgs.gov/of/2003/of03-372/.]

Castelao, R., O. Schofield, S. Glenn, R. Chant, and J. Kohut (2008), Cross-shelf transport of freshwater on the New Jersey shelf, *J. Geophys. Res.*, *113*, C07017, doi:10.1029/2007JC004241.

Chant, R. J., S. M. Glenn, E. Hunter, J. Kohut, R. F. Chen, R. H. Houghton, J. Bosch, and O. Schofield (2008), Bulge formation of a Buoyant River Outflow, *J. Geophys. Res.*, *113*, C01017, doi:10.1029/2007JC004100.

Fairall, C. W., E. F. Bradley, J. E. Hare, A. A. Grachev, and J. Edson (2003), Bulk parameterization of air–sea fluxes: Updates and verification for the COARE algorithm, *J. Clim.*, *16*, 571–591.

Freeland, G. L., D. J. Stanley, D. J. P. Swift, and D. N. Lambert (1981), The Hudson Shelf Valley: Its role in shelf sediment transport, *Mar. Geol. Quat. Geol.*, *42*, 399–427.

Freeland, H., and K. Denman (1982), A topographically controlled upwelling centre off Vancouver Island, *J. Mar. Res.*, *40*, 1069–1093.

Gong, D., J. T. Kohut, and S. M. Glenn (2010), Seasonal climatology of wind-driven circulation on the New Jersey shelf, *J. Geophys. Res.*, *115*, C04006, doi:10.1029/2009JC005520.

Han, G., D. V. Hansen, and J. A. Galt (1980), Steady-state diagnostic model of the New York Bight, *J. Phys. Oceanogr.*, 10, 1998–2020.

Harris, C. K., and R. P. Signell (1999), Circulation and sediment transport in the vicinity of the Hudson Shelf Valley, in *Proceedings of the Sixth International Conference on Estuarine and Coastal Modeling*, edited by M. L. Spaulding and H. L. Butler, pp. 380–394, Am. Soc. of Civ. Eng., N. Y.

Harris, C. K., B. Butman, and P. Traykovski (2003), Winter-time circulation and sediment transport in the Hudson Shelf Valley, *Cont. Shelf Res.*, *23*, 801–820.

Hickey, B. M. (1997), The response of a steep-sided, narrow canyon to time-variable wind forcing, *J. Phys. Oceanogr.*, *27*, 697–726.

Hsueh, Y. (1980), On the theory of deep flow in Hudson Shelf Valley, *J. Geophys. Res.*, *85*, 4913–4918.

Hsueh, Y., K. C. Chen, and G. O. Marmorino (1984), A numerical model of the time-dependent wintertime circulation of the New York Bight, *J. Geophys. Res.*, *89*, 673–684.

Johnson, E. R. (1978), Quasigeostrophic flow above sloping boundaries, *Deep Sea Res.*, *25*, 1049–1077.

Kämpf, J. (2006), Transient wind-driven upwelling in a submarine canyons, *J. Geophys. Res.*, *111*, C11011, doi:10.1029/2006JC003497.

Kampf, J. (2007), On the magnitude of upwelling fluxes in shelf-break canyons, *Cont. Shelf Res.*, *27*, 2211–2223.

Kampf, J. (2009), On the interaction of time-variable flows with a shelf-break canyon, *J. Phys. Oceanogr.*, *39*(1), 248–260, doi:10.1175/2008JPO3753.1.

Kampf, J. (2012), Lee effects of localized upwelling in a shelf-break canyon, *Cont. Shelf Res.*, *42*, 78–88, doi:10.1016/j.csr.2012.05.005.

Keller, G. H., D. Lambert, G. Rowe, and N. Staresinic (1973), Bottom currents in Hudson Canyon, *Science*, *180*, 181–193.

Killworth, P. D. (1978), Coastal upwelling and Kelvin waves with small longshore topography, *J. Phys. Oceanogr.*, *8*, 188–205.

Klinck, J. M. (1989), Geostrophic adjustment over submarine canyons, *J. Geophys. Res.*, *94*, 6133–6144.

Klinck, J. M. (1996), Circulation near submarine canyons: A modeling study, *J. Geophys. Res.*, *101*, 1211–1223.

Lavelle, J. W., G. H. Keller, and T. L. Clarke (1975), Possible bottom current response to surface winds in the Hudson Shelf Channel, *J. Geophys. Res.*, *80*, 1953–1956.

Lentz, S. J. (2008a), Observations and a model of the mean circulation over the Middle Atlantic Bight continental shelf, *J. Phys. Oceanogr.*, *38*, 1203–1221.

Lentz, S. J. (2008b), Seasonal variations in the circulation of the Middle Atlantic Bight continental shelf, *J. Phys. Oceanogr.*, *38*(7), 1486–1500.

Lentz, S. J., K. Shearman, S. Anderson, A. Plueddemann, and J. Edson (2003), The evolution of stratification over the New England shelf during the Coastal Mixing and Optics study, August 1996 - June 1997, *J. Geophys. Res.*, *108*(C1), 3008, doi:10.1029/2001JC001121.

Manning, J. P., L. Y. Oey, D. Packer, J. Vitaliano, T. W. Finneran, K. W. You, and S. Fromm (1994), Observations of bottom currents and estimates of resuspended sediment transport at the New York Bight 12-mile dumpsite, *J. Geophys. Res.*, 99, 10,221–10,239.

Mayer, D. A. (1982), The structure of circulation: MESA physical oceanographic studies in New York Bight, 2, *J. Geophys. Res.*, 87, 9579–9588.

Mayer, D. A., G. C. Han, and D. V. Hansen (1982), Circulati on in the Hudson Shelf Valley: MESA physical oceanographic studies in New York Bight, 1, *J. Geophys. Res.*, 87, 9563–9578.

Mirshak, R., and S. E. Allen (2005), Spin-up and the effects of a submarine canyon: Applications to upwelling in Astoria Canyon, *J. Geophys. Res.*, *110*, C02013, doi:10.1029/2004JC002578.

Nelsen, T. A., P. E. Gadd, and T. L. Clarke (1978), Wind-induced current flow in the upper Hudson Shelf Valley, *J. Geophys. Res.*, *83*, 6073–6082.

Noble, M., B. Butman, and E. Williams (1983), On the longshelf structure and dynamics of subtidal currents on the eastern United States continental shelf, *J. Phys. Oceanogr.*, *13*, 2125–2147.

Pawlowicz, R., R. Beardsley, and S. Lentz (2002), Classical tidal harmonic analysis including error estimates in MATLAB using T_Tide, *Comput. Geosci.*, *28*, 929–937.

Pettigrew, N. R., J. D. Irish, and R. C. Beardsley (1986), Field evaluations of a bottom-mounted acoustic Doppler profiler and conventional current meter moorings, in *Proceedings of the IEEE/OES Third Working Conference on Current Measurement*, edited by G. F. Appell, and W. E. Woodward, pp. 153–162, Institute of Electrical and Electronics Engineers, N. Y.

Plueddemann, A. J., S. J. Lentz, and E. A. Terray (2003), Comparison of five current meters in a tidally dominated flow, in *Proceedings of the IEEE/OES Seventh Working Conference on Current Measurement Technology*, edited by J. Rizoli, pp. 176–181, Institute of Electrical and Electronics Engineers, The Printing House, Stoughton, Wis.

Scully, M. E., and C. T. Friedrichs (2007), The importance of tidal and lateral asymmetries in stratification to residual estuarine circulation in partially-mixed estuaries, *J. Phys. Oceanogr.*, *37*, 1496–1511.

Scully, M. E., C. T. Friedrichs, and J. M. Brubaker (2005), Control of estuarine stratification and mixing by wind-induced straining of the estuarine density field, *Estuaries*, *28*, 321–326.

Shaw, W., J. H. Trowbridge, and A. J. Williams III (2001), Budgets of turbulent kinetic energy and scalar variance in the continental shelf bottom boundary layer, *J. Geophys. Res.*, *106*, 9551–9564.

She, J., and J. M. Klinck (2000), Flow near submarine canyons driven by constant winds, *J. Geophys. Res.*, *105*, 28,671–28,694.

Shearman, R. K., and S. J. Lentz (2003), Dynamics of mean and subtidal flow on the New England shelf, *J. Geophys. Res.*, *108*(C2), C02015, doi:10.1029/2002JC001417.

Shepard, F. P., R. F. Dill, and U. von Rad (1969), Physiography and sedimentary processes of La Jolla Submarine Fan and Fan-Valley, *Am. Assoc. Pet. Geol. Bull.*, *53*, 39–42.

Thieler, E. R., B. Butman, W. C. Schwav, M. A. Allison, N. W. Driscoll, J. P. Donnelly, and E. Uchupi (2007), A catastrophic meltwater flood event and the formation of Hudson Shelf Valley, *Palaeogeogr. Palaeoclimatol. Palaeoecol.*, *246*, 120–136.

Werner, S. R., R. C. Beardsley, S. J. Lentz, D. L. Herbert, and N. S. Oakey (2003), Observations and modeling of the tidal bottom boundary layer on the southern flank of Georges Bank, *J. Geophys. Res.*, *108*(C11), 8005, doi:10.1029/2001JC001271.

Wiberg, P. L., D. E. Drake, and D. A. Cacchione (1994), Sediment resuspension and bed armoring during high bottom stress events on the northern California continental shelf: measurements and predictions, *Cont. Shelf. Res.*, *14*, 1191–1291, doi:10.1016/0278-4343(94)90034-5.

Zhang, W. G., J. L. Wilkin, and R. J. Chant (2009), Modeling the pathways and mean dynamics of river plume dispersal in New York Bight, *J. Phys. Oceanogr.*, 39, 1167–1183.